AAS 25-244

MULTIPLE INTERIOR-POINT CONSTRAINTS FOR POWER-LIMITED OPERATIONAL COMPLIANT TRAJECTORIES

Alessandra Mannocchi[*] and Francesco Topputo[†]

Deep-space missions will be performed in the future by stand-alone CubeSats: for them, electric propulsion is a paramount option to enable their cost-effective space access. For limited budget reasons, these spacecraft need to follow operational compliant trajectories, alternating coasting and thrusting periods imposed at pre-defined time instants, the duty cycles. Moreover, the electrical power used varies with the heliocentric distance and drops to zero once a certain range is reached. Traditional trajectory optimization algorithms exhibit convergence problems when handling these discontinuous constraints. This work presents an optimal indirect method to compute power-limited operational compliant trajectories imposing multiple interior-point constraints, and its promising results.

INTRODUCTION

In the last few years, the space sector have been witnessing a significant reduction in space mission costs. An expression of this trend is the rapid development of CubeSat technology.[1] Several released-in-situ, deep-space CubeSat missions are expected to be launched in the next years by ESA (e.g., LUMIO,[2] Milani,[3] Juventas,[4] SATIS[5]). Similarly, deep-space stand-alone interplanetary CubeSats, able to travel to their final destination without the need of a carrying mothership, are expected to permeate the inner Solar System soon. The Miniaturised Asteroid Remote Geophysical Observer (M-ARGO)[6] will be the first European CubeSat to perform a similar mission towards a near-Earth asteroid (NEA).

High specific impulse values make solar electric propulsion (SEP) a good candidate for this kind of probe.[7] For SEP, the electrical power used to accelerate the propellant varies with heliocentric distance.[8] In turn, the thrust and specific impulse vary as a function of the input power. Incorporating an accurate SEP engine model into trajectory design radically improves mass budget estimation. However, this model includes additional constraints in the optimization. Due to technological reasons, the input power to the engine is limited, and the related bounded values are key thruster parameters: the spacecraft flies ballistically if insufficient power is provided, while the input power is capped at a maximum value when excess power is available.[9,10]

Electric propulsion also requires a significant effort from on-ground flight dynamics, with regularly scheduled navigation and guidance operations. This is particularly true for stand-alone deep-space CubeSats that, with stringent thrusting, power, and pointing budgets,[11] are unable to perform operations, such as communication, ground-based orbit determination and correction, or scientific experiments, while thrusting. To overcome these issues CubeSats will be required to follow

[*]PhD Student, DAER, Politecnico di Milano, Piazza Leonardo da Vinci, 32, 20133 Milano.
[†]Full Professor, DAER, Politecnico di Milano, Piazza Leonardo da Vinci, 32, 20133 Milano.

operational-compliant (OC) trajectories, consisting of a repetition of a regular pattern of alternating thrusting and coasting arcs (duty cycles). OC trajectories can be designed in any way necessary to ease ground operations, for example miming the working week (e.g., 7 days duty cycles, with 6 days of thrust and 1 day of coasting).

Electric propulsion trajectories are designed by formulating a low-thrust optimal trajectory problem (LOTP).[12,13] No analytic solutions exist for this problem, but several numerical techniques, traditionally divided into direct and indirect methods, have been developed to solve it.[14] In this work we focus on the indirect formulation, aiming at finding the solution of the necessary optimality conditions derived by the calculus of variations.[15,16] The solutions of an indirect formulation are computed through some sort of gradient methods leveraging on the first, and sometimes second-order derivatives of the problem, thus required to be differentiable at least up to the first order.[17]

Duty cycles are time-dependent and discontinuous constraints, and for this reason, they are not straightforward to introduce in indirect methods.[18] Their presence is usually ignored in the preliminary trajectory design phases. The convergence difficulty of indirect methods is also exacerbated by dynamics discontinuities when the input power is capped within bounds technologically lead. The homotopy technique, or continuation, is a class of methods conceived to deal with discontinuous structures in the LOTP. They allow the solution of the original, difficult, and discontinuous problem, starting from an easier one.[19] It is usually employed in indirect methods to overcome discontinuity problems as bang-bang control in fuel optimal solutions,[20,21] to impose varying maximum thrust models[22] and shutdown of the thruster due to eclipses.[23] Recently, the problem of forced coasting arcs imposition has become more and more relevant, and homotopic techniques have been employed to solve it[24–26] also in direct formulations.[27] However, it has not yet been coupled with the discontinuities introduced by the limited range of power input on a variable power SEP thruster.

In this work, a formulation based on the modeling of both the alternation of duty cycles and the power-limited SEP thruster as interior-point constraints is proposed. The solution method relies on the use of analytical derivatives, switching times detection techniques, and a four-layer continuation scheme rapidly generating power-limited and operational-compliant low-thrust trajectories. The main contribution of the work is the presentation of a method capable of modeling duty cycles with durations of any kind without any prior knowledge of the structure of the control law, as well as the introduction of a variable and limited power model for both specific impulse and thrust. The formulation is used to solve fuel optimal trajectories in the M-ARGO CubeSats scenario. The method proposed in this paper allows the computation of trajectories necessary for making deep-space CubeSat missions a reality soon.

PROBLEM STATEMENT

Theoretical Background

The equations of the dynamics of a spacecraft in cartesian coordinates in an interplanetary heliocentric two-body problem are

$$\dot{\mathbf{x}} = \mathbf{f}(\mathbf{x}, \boldsymbol{\alpha}, u) \Rightarrow \begin{cases} \dot{\mathbf{r}} = \mathbf{v} \\ \dot{\mathbf{v}} = -\frac{\mu}{r^3}\mathbf{r} + u\frac{T_{max}(r)}{m}\boldsymbol{\alpha} \\ \dot{m} = -u\frac{T_{max}(r)}{I_{sp}(r)g_0} \end{cases} \tag{1}$$

where $\mathbf{r}$, $\mathbf{v}$ and m are respectively the spacecraft position, velocity, and mass, and r is the norm of the position vector. The control is provided by the vector $\boldsymbol{\alpha}$, the thrust direction unit vector, and $u \in [0,1]$, the thrust throttle factor. The values μ and g_0 are the gravitational constant of the Sun and the Earth's gravitational acceleration at sea level. The specific impulse and the maximum thrust, I_{sp} and T_{max} respectively, are considered as functions of the input power to the engine P_{in}, which in turn is a function of the distance of the spacecraft with respect to the Sun r.

To include into the dynamics the policy of the engine due to the imposition of the duty cycles and of the power limitation, two switching functions influencing the throttle factor are defined. Firstly, $S_p = S_p(r)$ is defined as the power switching function used to detect the thruster operation logic according to

$$\text{if} \quad S_p(r) \geq P_{max} \quad \text{then} \quad P_{in} = P_{max}, \quad u \in [0,1] \tag{2}$$

$$\text{if} \quad S_p(r) \in [P_{min}, P_{max}) \quad \text{then} \quad P_{in} = S_p(r), \quad u \in [0,1] \tag{3}$$

$$\text{if} \quad S_p(r) < P_{min} \quad \text{then} \quad P_{in} = S_p(r), \quad u = 0 \tag{4}$$

where P_{max} and P_{min} are respectively the constant upper and lower bounds of power input to the engine, imposed by the technological constraints. The relation between the P_{in} and S_p is shown in Fig. 1. The S_p function is usually modeled as a polynomial in r.

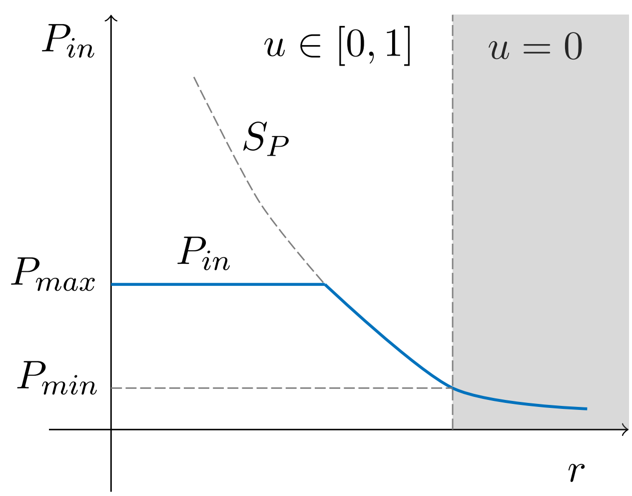

Figure 1. Relation between the P_{in} and S_P functions.

Secondly, in OC trajectory design the final goal is to switch off the electric engine according to a pre-defined duty cycle time-based schedule. To capture the logic of the enforced coasting arcs, the duty cycle switching function $S_{DC} = S_{DC}(t)$, is defined such that

$$\text{if} \quad S_{DC}(t) \geq \varepsilon_{DC} \quad \text{then} \quad u \in [0,1] \tag{5}$$

$$\text{if} \quad S_{DC}(t) < \varepsilon_{DC} \quad \text{then} \quad u = 0 \tag{6}$$

where ε_{DC} is a constant pre-defined threshold. It is worth noting that the function S_{DC} can have any continuous form as long as it is only a function of the time t. The LOTP aims at computing the optimal controls $\boldsymbol{\alpha}^*$ and u^* that minimizes J, a scalar cost function, under some boundary conditions at the initial and final times, t_i and t_f. If the objective is to save the propellant mass m_p, the LOTP is called a fuel-optimal (FO) problem, and the cost function is

$$J_f = \int_{t_i}^{t_f} \frac{T_{max}(r)}{I_{sp}(r) g_0} u \, \mathrm{d}t \tag{7}$$

while the boundary conditions are expressed as

$$\mathbf{r}(t_i) = \mathbf{r}_i; \quad \mathbf{v}(t_i) = \mathbf{v}_i \quad \text{and} \quad m(t_i) = m_i \tag{8}$$

$$\mathbf{r}(t_f) = \mathbf{r}_T(t_f) \quad \text{and} \quad \mathbf{v}(t_f) = \mathbf{v}_T(t_f) \tag{9}$$

where $\mathbf{r}_i$, $\mathbf{v}_i$ and m_i are the prescribed initial conditions of the probes $\mathbf{x}_i = [\mathbf{r}_i, \mathbf{v}_i, m_i]$, and $\mathbf{r}_T(t_f)$ and $\mathbf{v}_T(t_f)$ are the known position and velocity of the target at the final time, fixed in the case considered. The FO problem aims at computing the optimal control function $\mathbf{u}^* = [\boldsymbol{\alpha}^*, u^*]$ that minimizes J_f. It is known however[14] that the optimal control u^* of an FO solution exhibits a bang-bang, discontinuous profile, which makes the convergence of the solver difficult. A homotopy technique was introduced in Ref. (21) to smooth the control profile, and gradually introduce this discontinuity into the problem. The idea is to solve a LOTP having the following objective function

$$J_\varepsilon = \int_{t_i}^{t_f} L_\varepsilon(\mathbf{x}, \mathbf{u}) \, \mathrm{d}t = \int_{t_i}^{t_f} \frac{T_{max}(r)}{I_{sp}(r) g_0} [u - \varepsilon u(1-u)] \, \mathrm{d}t \tag{10}$$

where $\varepsilon = 1$ corresponds to an energy optimal (EO) problem, and $\varepsilon = 0$ corresponds to a FO problem. The problem is solved iteratively, gradually reducing ε and providing as an initial guess the solution to the previous problem, until $\varepsilon = 0$ is reached. To retrieve $\mathbf{u}^* = [\boldsymbol{\alpha}^*, u^*]$ the necessary conditions for optimality are derived by introducing the Lagrange multipliers, or costates, $\boldsymbol{\lambda} = [\boldsymbol{\lambda}_r, \boldsymbol{\lambda}_v, \lambda_m]$ associated to the states. The Hamiltonian function of the auxiliary problems for $\varepsilon \in [0, 1]$ reads

$$H_\varepsilon = L_\varepsilon + \boldsymbol{\lambda}^T \cdot \mathbf{f} = \boldsymbol{\lambda}_r \cdot \mathbf{v} - \frac{\mu}{r^3} \mathbf{r} \cdot \boldsymbol{\lambda}_v + u \frac{T_{max}(r)}{I_{sp}(r) g_0} \left(S_\varepsilon - \varepsilon + \varepsilon u \right) \tag{11}$$

where S_ε is the switching function for the EO problem, and is defined as $S_\varepsilon = 1 - \lambda_m - \lambda_v \frac{I_{sp}(r) g_0}{m}$. The Pontryagin minimum principle (PMP)[28] states that the control $\mathbf{u}^*$, to be optimal, has to minimize H_ε at any time instant. Accordingly, the optimal thrust direction $\boldsymbol{\alpha}^*$ is chosen as[29,30]

$$\boldsymbol{\alpha}^* = -\frac{\boldsymbol{\lambda}_v}{\lambda_v} \quad \text{if} \quad \lambda_v \neq 0 \tag{12}$$

where λ_v is the norm of $\boldsymbol{\lambda}_v$. The optimal thrust throttle factor u^* is determined by both the PMP and the constraints introduced in Eqs. (2)-(6)

$$u^* = \begin{cases} 0 & \text{if} \quad S_\varepsilon > \varepsilon \quad \text{or} \quad S_{DC} < \varepsilon_{DC} \quad \text{or} \quad S_p < P_{min} \\ \frac{\varepsilon - S_\varepsilon}{2\varepsilon} & \text{if} \quad |S_\varepsilon| \leq \varepsilon \quad \text{and} \quad S_{DC} \geq \varepsilon_{DC} \quad \text{and} \quad S_P \geq P_{min} \\ 1 & \text{if} \quad S_\varepsilon < -\varepsilon \quad \text{and} \quad S_{DC} \geq \varepsilon_{DC} \quad \text{and} \quad S_P \geq P_{min} \end{cases} \tag{13}$$

As $\boldsymbol{\alpha}^*$ and u^* depend on S_ε, and thus on both the state and costate $\mathbf{y} = [\mathbf{x}, \boldsymbol{\lambda}]$, to find the optimal control they have to be integrated for the whole trajectory. The augmented equations of the dynamics are then considered, where $\boldsymbol{\alpha}^*$ is substituted according to Eq. (12)

$$\dot{\mathbf{y}} = \mathbf{F}(\mathbf{y}) \Rightarrow \begin{cases} \dot{\mathbf{r}} = \mathbf{v} \\ \dot{\mathbf{v}} = -\frac{\mu}{r^3}\mathbf{r} - u^* \frac{T_{max}}{m} \frac{\boldsymbol{\lambda}_v}{\lambda_v} \\ \dot{m} = -u^* \frac{T_{max}}{I_{sp} g_0} \\ \dot{\boldsymbol{\lambda}}_r = -\frac{3\mu}{r^5} \left(\mathbf{r} \cdot \boldsymbol{\lambda}_v\right) \mathbf{r} + \frac{\mu}{r^3} \boldsymbol{\lambda}_v + \frac{u^* \lambda_v}{m} \mathbf{t}_r + \frac{(\lambda_m - 1 + \varepsilon) u^* - \varepsilon u^{*2}}{I_{sp} g_0} \left(\mathbf{t}_r - \mathbf{i}_r \frac{T_{max}}{I_{sp}}\right) \\ \dot{\boldsymbol{\lambda}}_v = -\boldsymbol{\lambda}_r \\ \dot{\lambda}_m = -\frac{u^* \lambda_v T_{max}}{m^2} \end{cases} \tag{14}$$

where the dependence of both T_{max} and I_{sp} on r has been dropped to ease the notation. In Eq. (14) the terms $\mathbf{t}_r$ and $\mathbf{i}_r$ represent respectively the derivative of T_{max} and I_{sp} with respect to $\mathbf{r}$

$$\mathbf{t}_r = \frac{\partial T_{max}(r)}{\partial \mathbf{r}} = \begin{cases} \frac{\partial T_{max}(r)}{\partial P_{in}} \frac{\partial P_{in}}{\partial r} \frac{\partial r}{\partial \mathbf{r}} & \text{if} \quad S_P < P_{max} \\ \mathbf{0}_{3\times 1} & \text{otherwise} \end{cases} \tag{15}$$

$$\mathbf{i}_r = \frac{\partial I_{sp}(r)}{\partial \mathbf{r}} = \begin{cases} \frac{\partial I_{sp}(r)}{\partial P_{in}} \frac{\partial P_{in}}{\partial r} \frac{\partial r}{\partial \mathbf{r}} & \text{if} \quad S_P < P_{max} \\ \mathbf{0}_{3\times 1} & \text{otherwise} \end{cases} \tag{16}$$

where $\partial r / \partial \mathbf{r} = \mathbf{r}/r$.

Multiple-interior Point Constraint

When u^* is substituted in Eqs. (14) according to the policy in Eq. (13), imposing the switching off of the engine when $S_{DC} < \varepsilon_{DC}$ and when $S_P < P_{min}$ may not be an optimal action, as this is not foreseen by the minimization of the Hamiltonian H_ε in the PMP. To satisfy the necessary conditions of optimality, these events will be treated in this work as multiple interior-point constraints.[12] According to the interior-point formulation,[12] at the time instant t_s, when S_{DC} crosses ε_{DC} or S_P crosses P_{min}, the following additional jump necessary conditions have to be satisfied

$$H_\varepsilon\left(t_s^-\right) = H_\varepsilon\left(t_s^+\right) - \pi \left.\frac{\partial S}{\partial t}\right|_{t_s} \tag{17}$$

$$\boldsymbol{\lambda}\left(t_s^-\right) = \boldsymbol{\lambda}\left(t_s^+\right) + \pi \left.\frac{\partial S}{\partial \mathbf{x}}\right|_{t_s} \tag{18}$$

where the scalar Lagrange multiplier π is introduced and S is substituted into S_{DC} when it crosses ε_{DC} and by S_P when it crosses P_{min}. Consider firstly the former case. It can be proved[24] that a closed form of π_{DC} can be computed as

$$\pi_{DC} = \left(\left. \frac{\partial S_{DC}}{\partial t} \right|_{t_s} \right)^{-1} \frac{T_{max}}{I_{sp} g_0} \left[\Delta u \left(S_\varepsilon \left(t_s \right) - \varepsilon \right) + \varepsilon \left(u \left(t_s^- \right)^2 - u \left(t_s^+ \right)^2 \right) \right] \tag{19}$$

where $\Delta u = u\left(t_s^-\right) - u\left(t_s^+\right)$. As S_{DC} depends only on time, the only discontinuity is present in the Hamiltonian function, while the costates remain continuous across ε_{DC}. Consider now the latter case. As S_P depends on the state when S_P crosses P_{min} there will be a discontinuity on both the Hamiltonian function and the costates. It can be proved[22] that also in this case a close form for π_P can be found as

$$\pi_P = \frac{T_{max}}{I_{sp} g_0} \Delta u \frac{S_\varepsilon \left(t_s \right) - \varepsilon + \varepsilon \left(u \left(t_s^- \right) + u \left(t_s^+ \right) \right)}{\dot{S}_P \left(t_s \right)} \tag{20}$$

where $\dot{S}_P = dS_P/dt = \left(\partial S_P / \partial \mathbf{r}\right) \mathbf{v}$. As S_P depends only on $\mathbf{r}$, the jump condition Eq. (18) applies only to λ_r. The existence of a closed form for both π_{DC} and π_P transforms a potential tedious multi-point boundary value problem usually generated by the interior-point constraints[31] back into a simpler two-point boundary value problem.

Shooting Problem

All of the theoretical formulation presented up to now describes a two-point boundary value problem where the only left unknown variable is the value of the costates at the initial time, $\boldsymbol{\lambda}_i = \boldsymbol{\lambda}\left(t_i\right)$. In particular, let $\mathbf{y}(t) = \boldsymbol{\varphi}_\varepsilon \left(\mathbf{y}_i = \left[\mathbf{x}_i,\, \boldsymbol{\lambda}_i \right],\, t_i,\, t \right)$ be the solution flow for a specific ε value of Eqs. (14) integrated from the initial time t_i to a generic time instant t, with $u = u^*$ provided by Eq. (13) and $\mathbf{x}_i$ provided by Eqs. (8). Every time S_P crosses P_{min} the value of $\boldsymbol{\lambda}_\mathbf{r}(t_s^+)$ is obtained through Eq. (18). The two-point boundary value problem read as

$$\text{Find } \boldsymbol{\lambda}_i^* \text{ such that } \mathbf{y}\left(t_f\right) = \boldsymbol{\varphi}_\varepsilon \left(\left[\mathbf{x}_i,\, \boldsymbol{\lambda}_i^* \right], t_i, t_f \right) \text{ satisfies } \begin{bmatrix} \mathbf{r}\left(t_f\right) - \mathbf{r}_T\left(t_f\right) \\ \mathbf{v}\left(t_f\right) - \mathbf{v}_T\left(t_f\right) \\ \lambda_m\left(t_f\right) \end{bmatrix} = \mathbf{0} \tag{21}$$

Synthetically, this problem is a zero-finding one, where the function to null is the flow $\mathbf{y}\left(t_f\right)$ with respect to the final boundary conditions and the variables to guess are the initial costates $\boldsymbol{\lambda}_i$.

SOLUTION METHOD

Four-layer Continuation Scheme

The discontinuities introduced by the throttle factor policy of Eq. (13) prevent the solver from reaching convergence. For this reason, a four-layer continuation scheme is implemented in this work. The scheme assembles two schemes previously developed by the authors to ensure the convergence of the problem, i.e., the Hyperbolic Tangent Smoothing (HTS)[22] and the N_{max}-continuation.[24] The two are briefly recapped here. The idea of the HTS is to replace $T_{max}(r)$ in all the above equations with $\tilde{T}_{max}(r, \rho)$ defined as

$$\tilde{T}_{max}(r,\rho) = \begin{cases} T_{max} \times h(r,\rho) = T_{max} \times \frac{1}{2} \left[\tanh \left(\frac{P_{in} - P_{min}}{\rho} \right) \right] & \text{if} \quad \rho > 0 \\ T_{max} & \text{if} \quad \rho = 0 \end{cases} \tag{22}$$

where ρ is a smoothing factor and P_{in} and P_{min} are expressed in Watts. The HTS works by gradually reducing the value of ρ from a positive value to 0, in order to smooth the jump in control due to S_P crossing P_{min}. To visualize the effect, see Fig. 2, where the variation of $\tilde{T}_{max}(r, \rho)$ with respect to P_{in} for different ρ values is shown. When $\rho > 0$, in Eq. (14) the term $\mathbf{t}_r$ is substituted by $\tilde{\mathbf{t}}_r$, defined as

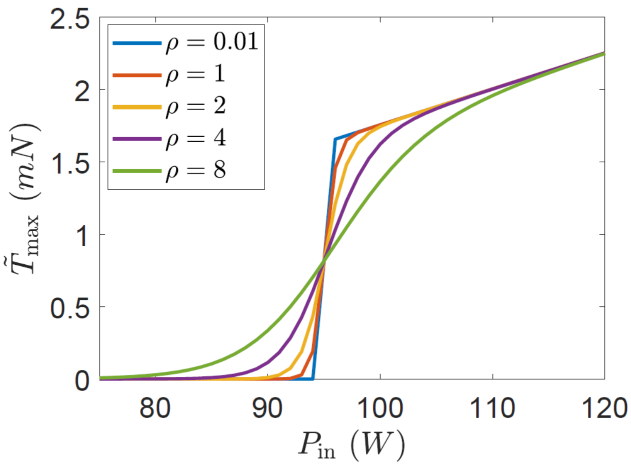

Figure 2. Variation of $\tilde{T}_{max}(r, \rho)$ with respect to P_{in} for different ρ values.

$$\tilde{\mathbf{t}}_r = \frac{\partial \tilde{T}_{max}(r)}{\partial \mathbf{r}} = \begin{cases} h(r,\rho)\mathbf{t}_r + T_{max}\frac{\partial h}{\partial \mathbf{r}} & \text{if} \quad S_P < P_{max} \\ \mathbf{0}_{3\times 1} & \text{otherwise} \end{cases} \tag{23}$$

where $\frac{\partial h}{\partial \mathbf{r}} = \frac{2h(1-h)}{\rho}\frac{\partial S_P}{\partial \mathbf{r}}$.

Consider now the N_{max}-continuation: it gradually turns inactive coasting arcs into active ones, i.e., the maximum number of forced coasting arcs N_{max} due to S_{DC} increases at each iteration of the continuation scheme. The N_{max} continuation is depicted in Fig. 3. The variable u_ζ is defined as the throttle factor in the N_{max}-th coasting arc to be imposed, and it is the last additional parameter on which a continuation is performed, if necessary. Starting from the FO solution (i.e., $N_{max} = 0$ and $u_\zeta = 0$), the number of active coasting arcs N_{max} is increased from 0 to 1. The FO solution is used as the initial guess for this auxiliary problem (i.e., $N_{max} = 1$ and $u_\zeta = 0$). Supposing the solution of this problem is obtained, N_{max} is increased from 1 to 2, and the new auxiliary problem is solved (i.e., $N_{max} = 2$ and $u_\zeta = 0$). Suppose that instead, in this case, the solver fails. Then u_ζ is imposed as 1, and the new problem is solved (i.e., $N_{max} = 2$ and $u_\zeta = 1$). The value of u_ζ is gradually reduced until $u_\zeta = 0$ is obtained. Starting from this solution as an initial guess, a new problem with $N_{max} = 3$ and $u_\zeta = 0$ is solved, and so on until the trajectory is OC.

Since the continuation on u_ζ foresees a minimum value of throttle factor, in general, different from 0, accordingly to the PMP,[23] the optimal throttle factor policy turns from Eq. (13) to

$$u^* = \begin{cases} u_{min} & \text{if} \quad S_\varepsilon > (1-2u_{min})\varepsilon \quad \text{or} \quad S_{DC} < \varepsilon_{DC} \quad \text{or} \quad S_p < P_{min} \\ \frac{\varepsilon - S_\varepsilon}{2\varepsilon} & \text{if} \quad -\varepsilon < S_\varepsilon \leq (1-2u_{min})\varepsilon \quad \text{and} \quad S_{DC} \geq \varepsilon_{DC} \quad \text{and} \quad S_P \geq P_{min} \\ 1 & \text{if} \quad S_\varepsilon < -\varepsilon \quad \text{and} \quad S_{DC} \geq \varepsilon_{DC} \quad \text{and} \quad S_P \geq P_{min} \end{cases} \tag{24}$$

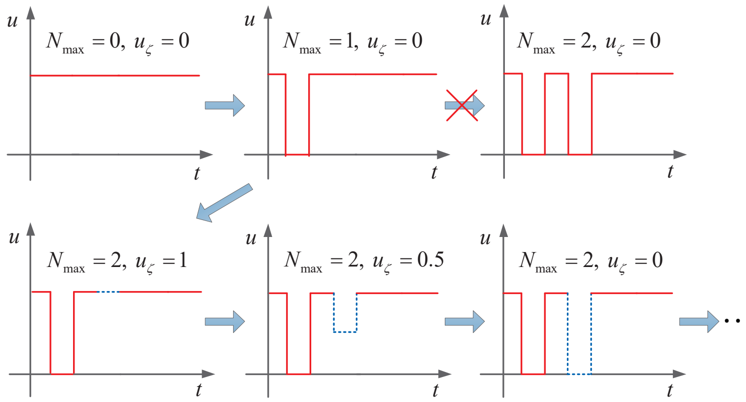

Figure 3. The N_{max}-continuation scheme.

where u_{min} is $u_\zeta = 1 \to 0$ in the N_{max}-the forced coasting arc, and 0 otherwise. The four-layer continuation is then a composition of the ε continuation from 1 to 0, i.e., from the EO to the FO solution, the HTS, and the N_{max}-continuation. The order of composition of these continuations is paramount to ease the convergence of the problem. Since very ill-conditioned derivative matrices (see next Subsection) are more likely to happen when several forced coasting arcs are present, the composition is chosen as performing the HTS firstly, secondly, the ε-continuation, and finally the N_{max}-continuation: in this way the discontinuity, and thus the ill-conditioning, would be encountered only at the final steps of the process.

Analytical Derivatives

To increase the accuracy and robustness of the computation, analytic derivatives of the shooting problem are computed. In particular from Eq. (14) the state transition matrix (STM) $\mathbf{\Phi}(t_i, t)$ is derived. The STM maps small variations in the initial conditions $\partial \mathbf{y}_i$ over a generic time instant $t > t_i$, i.e., $\partial \mathbf{y}(t) = \mathbf{\Phi}(t_i, t)\partial \mathbf{y}(t_i)$. The STM is subjected to the variational equation

$$\dot{\mathbf{\Phi}}(t, t_i) = D_y \mathbf{F} \mathbf{\Phi}(t, t_i) \quad \text{with} \quad \mathbf{\Phi}(t_i, t_i) = \mathbf{I}_{14x14} \tag{25}$$

where $D_y\mathbf{F}$ is the Jacobian matrix of $\mathbf{F}(\mathbf{y})$ and has six different expressions based on whether u^* is constant, ρ is 0, and $S_P < P_{max}$. Being subject to a variational equation, $\mathbf{\Phi}(t_i, t)$ has to be integrated with states and costates. Defining as $\mathbf{z} = [\mathbf{y}, \text{vec}(\mathbf{\Phi})]$ the 210-dimensional vector containing the 14 variables of $\mathbf{y}$ and the 196 elements of $\mathbf{\Phi}$, where the 'vec' operator converts a matrix into a vector, the integration to perform to solve the problem is

$$\dot{\mathbf{z}} = \mathbf{G}(\mathbf{z}) \Rightarrow \begin{cases} \dot{\mathbf{y}} = \mathbf{F}(\mathbf{y}) \\ \text{vec}(\dot{\mathbf{\Phi}}) = \text{vec}(D_y \mathbf{F} \mathbf{\Phi}) \end{cases} \tag{26}$$

However, $\mathbf{\Phi}$ maps states and costates along a continuous trajectory, and the bang-bang profile given by Eq. (13) creates discontinuities in it. At each switching time t_s, compensations in the STM, $\mathbf{\Psi}(t_s)$, must be added using the chain rule[32]

$$\mathbf{\Phi}(t_f, t_i) = \mathbf{\Phi}(t_f, t_N^+)\mathbf{\Psi}(t_N)\mathbf{\Phi}(t_N^-, t_{N-1}^+)\mathbf{\Psi}(t_{N-1}) \ldots \mathbf{\Phi}(t_2^-, t_1^+)\mathbf{\Psi}(t_1)\mathbf{\Phi}(t_1^-, t_i) \tag{27}$$

where N is the total number of discontinuities. Suppose that a discontinuity is detected at t_s for the switching function S_f crossing 0, and thus for the optimal control u^* jumping from 0 to 1 or vice versa. In this case $\mathbf{y}$ is continuous, but $\dot{\mathbf{y}}$ is discontinuous, and it can be proved[22] that the compensation matrix $\mathbf{\Psi}_f(t_s)$ is given by

$$\mathbf{\Psi}_f(t_s) = \frac{\partial \mathbf{y}(t_s^+)}{\partial \mathbf{y}(t_s^-)} = \mathbf{I}_{14x14} + (\dot{\mathbf{y}}(t_s^+) - \dot{\mathbf{y}}(t_s^-))\frac{1}{\dot{S}_f}\frac{\partial S_f}{\partial \mathbf{y}} \tag{28}$$

where $\dot{S}_f$ is the time derivative of the optimal switching function. Suppose instead that the jump for u^* from 0 to 1 or vice versa at t_s is due to the switching function S_{DC} crossing ε_{DC}. Also in this case $\mathbf{y}$ is continuous and $\dot{\mathbf{y}}$ is discontinuous, but no compensation matrix is needed. Indeed, since $\partial S_{DC}/\partial \mathbf{y} = \mathbf{0}$, it results that

$$\mathbf{\Psi}_{DC}(t_s) = \frac{\partial \mathbf{y}(t_s^+)}{\partial \mathbf{y}(t_s^-)} = \mathbf{I}_{14x14} \tag{29}$$

Indeed $\mathbf{\Psi}(t_s)$ maps variations of $\mathbf{y}(t_s^-)$ in variations in $\mathbf{y}(t_s^+)$, and S_{DC} does not depends on the $\mathbf{y}$, but only on time. Therefore, during the integration of Eq. (26), no corrections to the STM are necessary for switching in S_{DC}. Finally, consider the switching imposed by S_P trespassing P_{min} and P_{max}. In the latter case, again $\mathbf{y}$ is continuous, but $\dot{\mathbf{y}}$ is discontinuous. It can be proved[22] that the compensation matrix $\mathbf{\Psi}_{P_{max}}(t_s)$ is given by Eq. (28) where instead of S_f, the power switching function S_P is considered. Instead, when S_P crosses P_{min}, both $\mathbf{y}$ and $\dot{\mathbf{y}}$ are discontinuous, and the compensation matrix is given by[22]

$$\mathbf{\Psi}_{P_{min}}(t_s) = \frac{\partial \mathbf{y}(t_s^+)}{\partial \mathbf{y}(t_s^-)} = \mathbf{I}_{14x14} + \frac{\partial \Delta \mathbf{y}}{\partial \mathbf{y}} + (\dot{\mathbf{y}}(t_s^+) - \dot{\mathbf{y}}(t_s^-) - \Delta\dot{\mathbf{y}})\frac{1}{\dot{S}_P}\frac{\partial S_P}{\partial \mathbf{y}} \tag{30}$$

where $\Delta \mathbf{y}$ is the jump in $\mathbf{y}$ due to the interior point constraint of Eq. (18), and it is defined as $\Delta \mathbf{y} = [\mathbf{0}_{7\times 1}, \Delta\lambda_{\mathbf{r}}, \mathbf{0}_{4\times 1}]$, being $\Delta\lambda_{\mathbf{r}} = -\pi_P\,(\partial S_P/\partial \mathbf{r})$.

RESULTS

Switching Functions Modeling

Firstly, the modeling of the two switching functions S_{DC} and S_P is presented. The duty cycle switching function $S_{DC} = S_{DC}(t)$, depending only on time, has to be properly modeled to impose the correct duration of each forced coasting arc. This is performed by modeling it as a pulse wave function, being similar to the thrust profile desired. In particular, due to its regularity and smoothness with respect to the normal pulse wave function, an expansion based on the sinc function $\mathrm{sinc}(t) = \sin(\pi t)/\pi t$ is employed as

$$S_{DC}(t) = \frac{A\tau}{T}\left(1 + 2\sum_{n=1}^{\infty}\left(\mathrm{sinc}\left(n\frac{\tau}{T}\right)\cos\left(2\pi n f t\right)\right)\right) \tag{31}$$

where A is the amplitude, T is the period, τ is the pulse length, and $f = 1/T$ is the frequency of the pulse wave. These values are customized in order to enforce the right duration of the coasting arcs, e.g., to have duty cycles corresponding to a working week with 6 days of thrusting and 1 day of coasting, T is imposed to be 7 days, and τ to be 6 days (see Fig. 4(a) for reference). The expansion

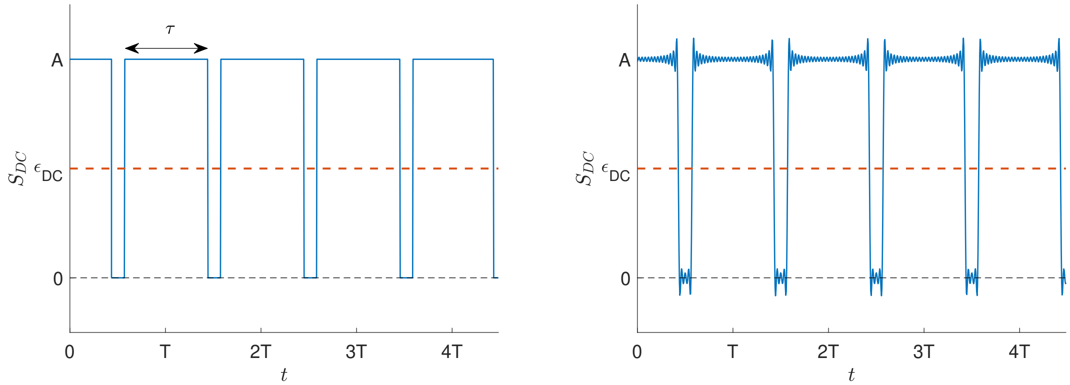

(a) *Pulse wave modeling the duty cycles alternation.* (b) *Pulse wave modeling with sinc expansion.*

Figure 4. Duty cycle switching function modeling as a pulse wave.

of the wave is truncated at a value $n = 30$ in order to have smoothness in the function (see Fig. 4(b)), and ε_{DC} is set to be half the value of the amplitude A, which is set to 0.2.

The power switching function S_P instead, and the function expressing T_{max} and I_{sp} as function of the input power P_{in}, are handled using fourth-order polynomials

$$S_P(r) = c_0 + c_1 r + c_2 r^2 + c_3 r^3 + c_4 r^4 \tag{32}$$

$$T_{max}(P_{in}) = a_0 + a_1 P_{in} + a_2 P_{in}^2 + a_3 P_{in}^3 + a_4 P_{in}^4 \tag{33}$$

$$I_{sp}(P_{in}) = b_0 + b_1 P_{in} + b_2 P_{in}^2 + b_3 P_{in}^3 + b_4 P_{in}^4 \tag{34}$$

where the coefficients a_i, b_i and c_i are listed in the next section, and in general depend on the engine used, being retrieved by experimental testings. The variations of S_P, T_{max}, and I_{sp} are reported in Fig. 5. Note that the theoretical foundation for the modeling of both switching functions remains valid as long as the dependence on the same variables is kept (t for S_{DC} and $\mathbf{r}$ for S_P). This means that different shapes of duty cycles or different engines can be used with the proposed method to compute power-limited operational-compliant trajectories.

Numerical Simulations

The simulations in this subsection have been solved with a normalization of the variables involved with the constants listed in Table 1. The simulations have been performed with an Intel i9-9980HK, a total RAM of 16 GB, and Matlab R2023b. The integration code is converted to MEX to speed up simulations. To perform the continuation in ε, it has been imposed a variation $\Delta\varepsilon = 0.05$, while for ρ is chosen an initial value of 4 and a variation $\Delta\rho = 0.5$, and for u_ζ a variation $\Delta u_\zeta = 0.1$. The continuations fail if $\Delta u_\zeta < 0.005$, $\Delta\varepsilon < 10^{-8}$, or $\Delta\rho < 0.01$. The integrations used to solve the shooting problems are performed using a variable-step 7^{th}-8^{th} Runge–Kutta integration scheme, where it has been imposed an integration tolerance of 10^{-11} and a maximum integration step in order to have at least 3 nodes into each coasting arc.

The scenario assumed is the M-ARGO CubeSat one. The assumptions for the simulations are reported in Table 2. The ephemerides of the asteroid 2010 UE51 are retrieved from the Spacecraft

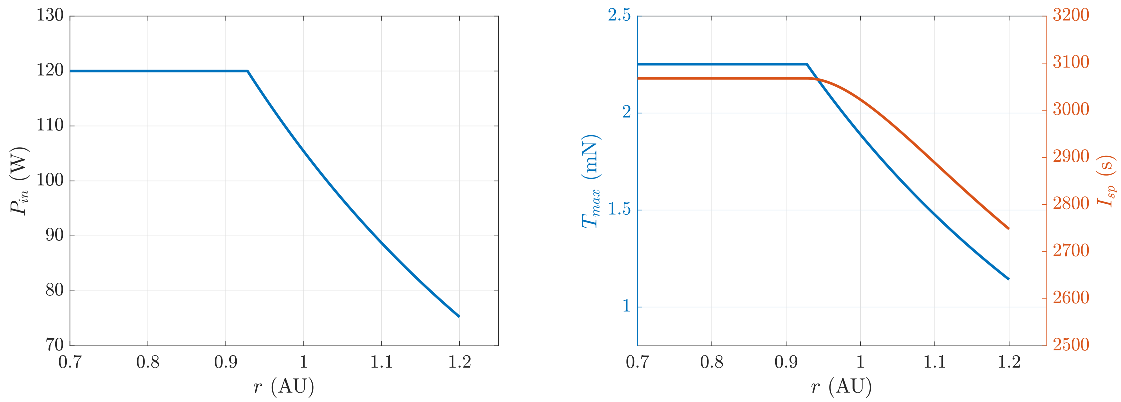

(a) *Input power over heliocentric distance.*

(b) *Maximum thrust and specific impulse over heliocentric distance.*

Figure 5. Polynomials representing the performance of the engine.

Table 1. Constants used in the normalization.

Parameter	**Value**
Sun gravitational constant, μ	1.327124×10^{11} km^3/s^2
Earth gravitational acceleration, g_0	9.80665 m/s^2
Length unit LU	1.495978×10^{8} km
Time unit TU	5.022643×10^{6} s
Velocity unit VU	29.784692 km/s
Mass unit MU	28.2 kg
Force unit FU	0.142322 N
Power unit PU	4.980840×10^{3} W

Planet Instrument Camera-matrix Events (SPICE) kernels of the HORIZONS system.[33] The departure date is set the 17^{th} September 2023, with a time of flight of 581 days. The CubeSat is supposed to depart from the Sun–Earth L2 Lagrangian point, and to rendez-vou with the asteroid. The values of the coefficients in the polynomials of Eqs. (32)-(34) are reported in Table 3.

The FO solution with the variable engine model and no duty cycle imposition is reported in Figs. 6(a) and 6(b). To have this solution as baseline confrontation for the other solutions, the values of P_{min} = 80 W and P_{max} = 120 W have been imposed: note that those are indeed the nominal values of the engine model selected, and they do not trigger the HTS continuation. In Fig. 7 the profiles of the variable power, maximum thrust, and specific impulse of the FO solution are reported as well. Note that the fuel consumption of this trajectory is 1.076004 kg.

To test the efficacy of the method proposed, several simulations triggering different values of input power have been performed. For a preliminary analysis, the duty cycle scheme is set to T = 20 days and τ = 18 days. The results of the simulations are reported in Table 4. The trajectories in the J2000 reference frame as well as the profiles of input power, maximum thrust, and specific impulse of these solutions are not reported as they are all very similar to the one in Fig. 6(a).

The four solutions show similar computational times, the higher being solution C. Note that so-

Table 2. Scenario assumptions.

Parameter	Value
Asteroid	2010 UE51
Departure date	17 September 2023
Time of flight	581 days
m_0	28.2 kg
T	20 days
τ	18 days

Table 3. Coefficients of the polynomial for the performance of the engine.

P_{in}	I_{sp}	T_{max}
c_0 = 840.11 W	b_0 = 2652 s	a_0 = -0.7253 mN
c_1 = -1754.3 W/LU	b_1 = -18.123 s/W	a_1 = 0.02481 mN/W
c_2 = 1625.01 W/LU^2	b_2 = 0.3887 s/W^2	a_2 = 0 mN/W^2
c_3 = -739.87 W/LU^3	b_3 = -0.00174 s/W^3	a_3 = 0 mN/W^3
c_4 = 134.45 W/LU^4	b_4 = 0 s/W^4	a_4 = 0 mN/W^4

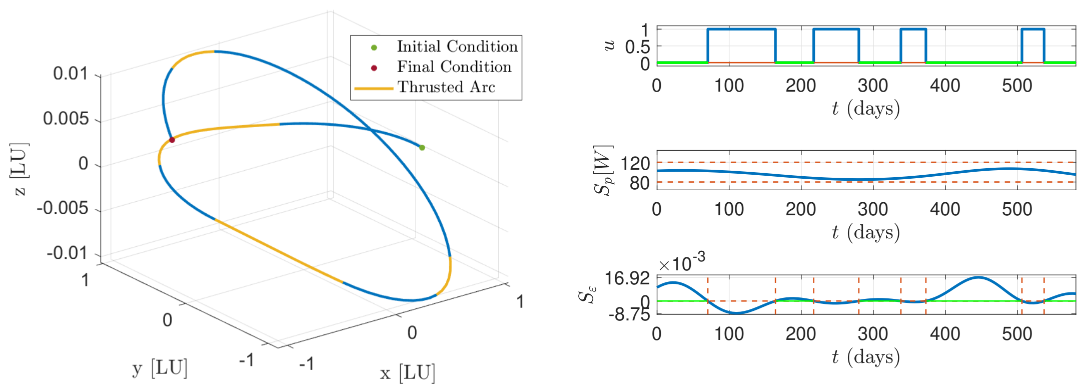

(a) *Trajectory in the J2000 reference frame.* (b) *Throttle factor, S_P, and S_ε profiles.*

Figure 6. FO reference solution trajectory.

lution D triggers all the values of all the switching functions. In Table 4, the increment in propellant mass $\Delta\, m_p$ is computed with respect to the reference value of 1.076004 kg of the FO solution. It can be noted that the highest increments belong to solutions B and D. It is an expected result as these solutions have a higher P_{min} and thus impose longer switching off of the engine, with respect to A and C, where reaching P_{max} means just a cap on the maximum thrust and specific impulse. All the solutions, however, have a $\Delta\, m_p$ lower than 3.5 %.

In Figs. from 8 to 9 the throttle factor u, S_{DC}, S_P, and S_ε for each solution have been reported. The brilliant green lines highlight where the switching off of the engine is imposed by the optimality of the solution, i.e., where $S_\varepsilon > 0$. The yellow lines highlight where the switching off of the engine is imposed by insufficient input power, i.e., where $S_P < P_{min}$.

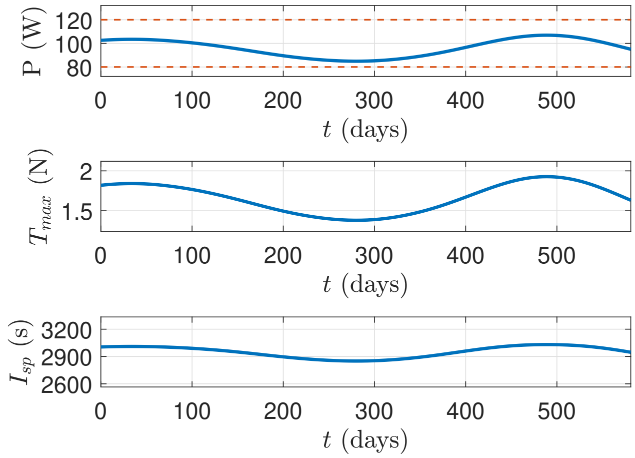

Figure 7. Input power, T_{max}, and I_{sp} of the FO solution.

Table 4. Summary of the results of the simulations.

Solution	P_{min} (W)	P_{max} (W)	$\mathbf{m_p}$ (kg)	$\mathbf{\Delta}$ $\mathbf{m_p}$ (%)	**CPU time** (s)
A	80	120	1.076380	0.0350	12.11
B	90	120	1.112183	3.3624	14.63
C	80	105	1.076410	0.0461	28.95
D	90	105	1.112714	3.4118	14.94

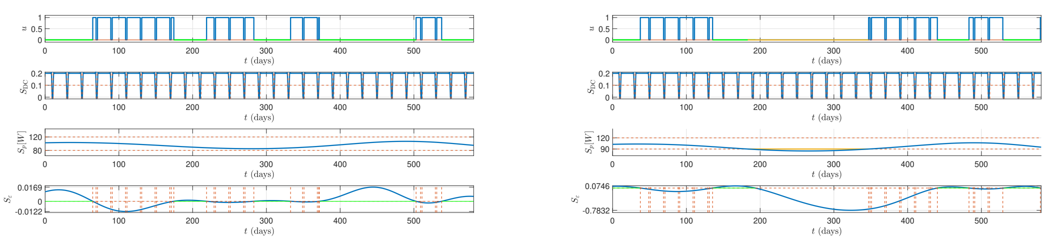

(a) *Solution A, with P_{min} = 80 W and P_{max} = 120 W.* (b) *Solution B, with P_{min} = 90 W and P_{max} = 120 W.*

Figure 8. Solutions A and B, with P_{max} = 120 W, and P_{min} = 80 W and P_{min} = 90 W, respectively.

Remarkably, all the throttle factor profiles show the same structure of 4 main thrusting periods, coming from the FO solution. Solutions B and D however, show only 3, as the switching off of the engine for insufficient input power eliminates one thrusting possibility.

In Fig. 10 it has been reported the profile of the costate $\boldsymbol{\lambda}_r$ for solution D. Around day 350 a jump in the value of the costate can be noted. This is in accordance with the jump conditions of Eq. (18) as at that instant the input power crosses P_{min} (visible in Fig. 9(b)). Accordingly, also, no jump can be appreciated around 200, when firstly the input power crosses P_{min}. Indeed, the engine is already off for $S_\varepsilon > \varepsilon$, and thus no discontinuity in $\mathbf{y}$ is experienced, as expected.

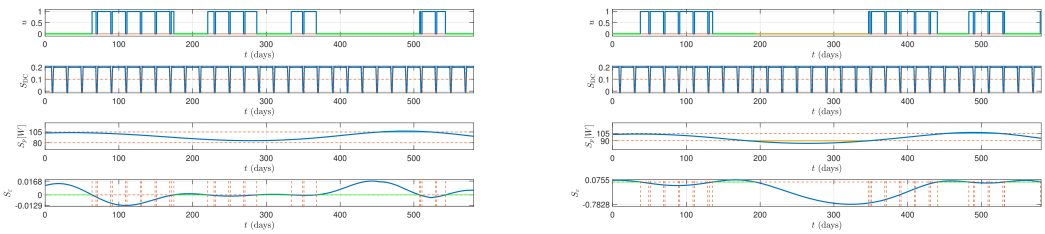

(a) *Solution C, with P_{min} = 80 W and P_{max} = 105 W.* (b) *Solution D, with P_{min} = 90 W and P_{max} = 105 W.*

Figure 9. Solutions C and D, with P_{max} = 105 W, and P_{min} = 80 W and P_{min} = 90 W, respectively.

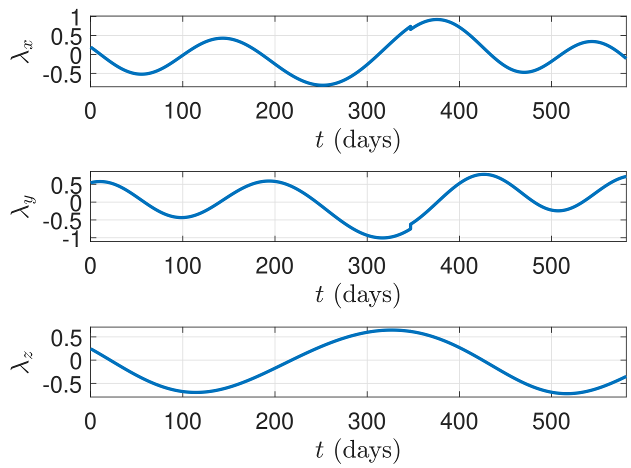

Figure 10. Profile of the costate λ_r for solution D.

CONCLUSION

In this work, the problem of operationally compliant trajectories is investigated. The problem includes the imposition of duty cycles, a pre-defined alternation of thrusting and forced coasting arcs, and a limited-and-variable power engine model. A novel formulation of these constraints in indirect trajectory optimization is presented, formulated as multiple-interior point constraints.

The optimization is based on a four-layer continuation scheme and the use of analytic derivatives for robustness and accuracy. The necessary conditions for optimality are derived for the fuel optimal problem, as well as the multiple jump conditions in the Hamiltonian and in the Lagrangian costates. The proposed method is applied to the M-ARGO CubeSat scenario. Through several tests, it is proven to generate trajectories in a fast way, without any need for prior knowledge of the thrust profile. The solutions are shown to respect the mathematical formulation derived. Moreover, they are similar in thrusting profiles to the fuel optimal solutions without constraints and show increments in propellant mass with respect to this last one lower than 3.5 %.

This method allows the design of trajectories paramount for the future mission design of interplanetary stand-alone CubeSat missions.

ACKNOWLEDGMENT

This project has received funding from the European Research Council (ERC) under the European Union's Horizon 2020 research and innovation program (grant agreement No. 864697).

A. Mannocchi and F. Topputo would also like to acknowledge the funding received under ESA Contracts No. 4000136010/21/NL/GLC/my.

REFERENCES

[1] R. Walker, D. Binns, C. Bramanti, M. Casasco, P. Concari, D. Izzo, D. Feili, P. Fernandez, J. G. Fernandez, P. Hager, D. Koschny, V. Pesquita, N. Wallace, I. Carnelli, M. Khan, M. Scoubeau, and D. Taubert, "Deep-space CubeSats: thinking inside the box," *Astronomy & Geophysics*, Vol. 59, No. 5, 2018, pp. 5.24–5.30, 10.1093/astrogeo/aty232.

[2] A. Cervone, F. Topputo, S. Speretta, A. Menicucci, E. Turan, P. Di Lizia, M. Massari, V. Franzese, C. Giordano, G. Merisio, *et al.*, "LUMIO: A CubeSat for observing and characterizing micro-meteoroid impacts on the Lunar far side," *Acta Astronautica*, Vol. 195, 2022, pp. 309–317, 10.1016/j.actaastro.2022.03.032.

[3] F. Ferrari, V. Franzese, M. Pugliatti, C. Giordano, and F. Topputo, "Trajectory options for Hera's Milani CubeSat around (65803) Didymos," *The Journal of the Astronautical Sciences*, Vol. 68, No. 4, 2021, pp. 973–994, 10.1007/s40295-021-00282-z.

[4] H. R. Goldberg, Ö. Karatekin, B. Ritter, A. Herique, P. Tortora, C. Prioroc, B. G. Gutierrez, P. Martino, and I. Carnelli, "The Juventas CubeSat in support of ESA's Hera mission to the asteroid Didymos," *Proceedings of the Small Satellite Conference*, Vol. 1 of *SSC19-WKIV-05*, Utah State University, Logan, UT, 2019.

[5] Ö. Karatekin, B. Ritter, B. Gundlach, C. Güttler, M. Patzek, F. Cabral, D. Catisanu, V. Fogliano, P. Holsters, R. Walker, *et al.*, "Satis Mission Study for Apophis: Science Objectives and Mission Definition," *LPI Contributions*, Vol. 3006, 2024, p. 2043.

[6] F. Topputo, Y. Wang, C. Giordano, V. Franzese, H. Goldberg, F. Perez-Lissi, and R. Walker, "Envelop of reachable asteroids by M-ARGO CubeSat," *Advances in Space Research*, Vol. 67, No. 12, 2021, pp. 4193–4221, 10.1016/j.asr.2021.02.031.

[7] J. C. Pascoa, O. Teixeira, and G. Filipe, "A review of propulsion systems for CubeSats," *ASME International Mechanical Engineering Congress and Exposition*, Vol. 1 of *V001T03A039*, Pittsburg, PA, 2018, 10.1115/IMECE2018-88174.

[8] S. N. Williams and V. Coverstone-Carroll, "Benefits of solar electric propulsion for the next generation of planetary exploration missions," *The Journal of the Astronautical Sciences*, Vol. 45, 1997, pp. 143–159, 10.1007/BF03546373.

[9] D. Y. Oh, "Evaluation of solar electric propulsion technologies for discovery-class missions," *Journal of Spacecraft and Rockets*, Vol. 44, No. 2, 2007, pp. 399–411, 10.2514/1.21613.

[10] R. Woolley and Z. Olikara, "Optimized low-thrust missions from GTO to Mars," *2019 IEEE Aerospace Conference*, IEEE, 2019, pp. 1–10, 10.1109/AERO.2019.8741558.

[11] T. J. Martin-Mur, E. D. Gustafson, and B. T. Young, "Interplanetary CubeSat navigational challenges," *25th International Symposium on Space Flight Dynamics (ISSFD)*, Munich, Germany, 2015.

[12] A. Bryson and Y.-C. Ho, *Applied optimal control*. London: Taylor & Francis, 1975, 10.1201/9781315137667.

[13] D. G. Hull, *Optimal control theory for applications*. Berlin, Germany: Springer Science & Business Media, 2013, 10.1007/978-1-4757-4180-3.

[14] J. T. Betts, "Survey of Numerical Methods for Trajectory Optimization," *Journal of Guidance, Control, and Dynamics*, Vol. 21, No. 2, 1998, pp. 193–207, 10.2514/2.4231.

[15] J. A. Kechichian, "Optimal low-Earth-orbit-geostationary-Earth-orbit intermediate acceleration orbit transfer," *Journal of Guidance, Control, and Dynamics*, Vol. 20, No. 4, 1997, pp. 803–811, 10.2514/2.4116.

[16] C. L. Ranieri and C. A. Ocampo, "Indirect optimization of three-dimensional finite-burning interplanetary transfers including spiral dynamics," *Journal of Guidance, Control, and Dynamics*, Vol. 32, No. 2, 2009, pp. 445–455, 10.2514/1.38170.

[17] D. Morante, M. Sanjurjo Rivo, and M. Soler, "A survey on low-thrust trajectory optimization approaches," *Aerospace*, Vol. 8, No. 3, 2021, p. 88, 10.3390/aerospace8030088.

[18] T. Li, Z. Wang, and Y. Zhang, "Double-homotopy technique for fuel optimization of power-limited interplanetary trajectories," *Astrophysics and Space Science*, Vol. 364, No. 9, 2019, pp. 1–12, 10.1007/s10509-019-3637-6.

[19] F. Jiang, H. Baoyin, and J. Li, "Practical techniques for low-thrust trajectory optimization with homotopic approach," *Journal of Guidance, Control, and Dynamics*, Vol. 35, No. 1, 2012, pp. 245–258, 10.2514/1.52476.

[20] R. Bertrand and R. Epenoy, "New smoothing techniques for solving bang–bang optimal control problems—numerical results and statistical interpretation," *Optimal Control Applications and Methods*, Vol. 23, No. 4, 2002, pp. 171–197, 10.1002/oca.709.

[21] R. Epenoy and R. Bertrand, "Optimal control and smoothing techniques for computing minimum fuel orbital transfers and rendezvous," *18th International Symposium on Space Flight Dynamics (ISSFD)*, Vol. 548, Munich, Germany, 2004, pp. 131–136.

[22] Y. Wang and F. Topputo, "Indirect optimization of power-limited asteroid rendezvous trajectories," *Journal of Guidance, Control, and Dynamics*, Vol. 45, No. 5, 2022, pp. 131–136, 10.2514/1.G006179.

[23] Y. Wang and F. Topputo, "Indirect optimization of fuel-optimal many-revolution low-thrust transfers with eclipses," *IEEE Transactions on Aerospace and Electronic Systems*, Vol. 59, No. 1, 2022, pp. 39–51, 10.1109/TAES.2022.3189330.

[24] A. Mannocchi, C. Giordano, and F. Topputo, "An Indirect Formulation of Operational Compliant Low-thrust Trajectories," *AIAA Scitech 2024 Forum*, 2024, p. 0631, 10.2514/6.2024-0631.

[25] R. Epenoy, "Fuel optimization of low-thrust trajectories under thrust and coast times constraints: a novel indirect approach," *Acta Astronautica*, Vol. 206, 2023, pp. 218–232, 10.1016/j.actaastro.2023.02.030.

[26] N. P. Nurre and E. Taheri, "Duty-cycle-aware low-thrust trajectory optimization using embedded homotopy," *Acta Astronautica*, Vol. 212, 2023, pp. 630–642, 10.1016/j.actaastro.2023.08.022.

[27] A. Mannocchi, C. Giordano, and F. Topputo, "A Homotopic Direct Collocation Approach for Operational-Compliant Trajectory Design," *The Journal of the Astronautical Sciences*, 2022, pp. 1–17, 10.1007/s40295-022-00351-x.

[28] B. A. Conway, "A Survey of Methods Available for the Numerical Optimization of Continuous Dynamic Systems," *Journal of Optimization Theory and Applications*, Vol. 152, 2012, pp. 271–306, 10.1016/j.asr.2008.01.011.

[29] B. A. Conway, *Spacecraft trajectory optimization*. Cambridge, UK: Cambridge University Press, 2010, 10.1017/CBO9780511778025.

[30] J. M. Longuski, J. J. Guzmán, and J. E. Prussing, *Optimal control with aerospace applications*. Berlin, Germany: Springer, 2014, 10.1007/978-1-4614-8945-0.

[31] T. Guo, J. Li, H. Baoyin, and F. Jiang, "Pseudospectral Methods for Trajectory Optimization with Interior Point Constraints: Verification and Applications," *IEEE Transactions on Aerospace and Electronic Systems*, Vol. 49, No. 3, 2013, pp. 2005–2017, 10.1109/TAES.2013.6558034.

[32] R. P. Russell, "Primer vector theory applied to global low-thrust trade studies," *Journal of Guidance, Control, and Dynamics*, Vol. 30, No. 2, 2007, pp. 460–472, 10.2514/1.22984.

[33] J. D. Giorgini and D. K. Yeomans, "On-line system provides accurate ephemeris and related data," Tech. Rep. NPO-20416, NASA, 1999.